



Journal of Geophysical Research: Space Physics

RESEARCH ARTICLE

10.1029/2018JA025290

Key Points:

- Two-dimensional magnetotail configurations with a B_Z hump may be MHD unstable
- Background pressure, entropy reduction, and initial hump location govern progression toward Earth
- Earthward propagating hump resembles dipolarization fronts generated by reconnection

Correspondence to:

J. Birn.

jbirn@spacescience.org

Citation

Birn, J., Merkin, V. G., Sitnov, M. I., & Otto, A. (2018). MHD stability of magnetotail configurations with a B_Z hump. Journal of Geophysical Research: Space Physics, 123, 3477–3492. https://doi.org/10.1029/2018JA025290

Received 30 JAN 2018 Accepted 1 APR 2018 Accepted article online 16 APR 2018 Published online 6 MAY 2018 Corrected 16 JUL 2018

This article was corrected on 16 JUL 2018. See the end of the full text for details.

MHD Stability of Magnetotail Configurations With a B_z Hump

J. Birn^{1,2}, V. G. Merkin³, M. I. Sitnov³, and A. Otto⁴

¹ Space Science Institute, Boulder, CO, USA, ²Los Alamos National Laboratory, Los Alamos, NM, USA, ³The Johns Hopkins University Applied Physics Laboratory, Laurel, MD, USA, ⁴University of Alaska Fairbanks, Fairbanks, AK, USA

Abstract Using two-dimensional magnetohydrodynamic (MHD) simulations, we explore the stability of magnetotail configurations that include a local enhancement of B_z (a " B_z hump"). We demonstrate that hump configurations can become unstable within the constraints of ideal MHD, even when strict boundary conditions $\mathbf{v}=0$ are imposed at all boundaries, consistent with the constraints of the ideal MHD energy principle. Necessary conditions for instability are that the boundaries on the earthward and high-latitude sides are far enough away, that the background pressure, equivalent to the lobe pressure, is small enough, and that the B_z enhancement or entropy reduction is strong enough. The unstable evolution then bears strong similarity to the evolution of observed and simulated dipolarized flux bundles and dipolarization fronts, presumed or simulated to be the consequence of reconnection. The B_z humps, which for sufficiently low background pressure correspond to entropy depletions, move faster for lower background density and penetrate closer toward Earth when they are initiated closer to Earth or when the background pressure is lower, similar to 3-D low-entropy flux tubes, which are affected by ballooning-/interchange-type modes.

1. Introduction

The enhancement of the normal magnetic field component B_n (or B_z) in the near and midtail, also called "dipolarization," is a common characteristic of magnetotail activity, including, but not limited to, magnetospheric substorms. In the tail region between approximately 10 and 25 R_E distance such events are typically associated with a sudden rise of positive B_z , commonly denoted as "dipolarization front" (Nakamura et al., 2002; Runov et al., 2009), followed by a brief interval of enhanced B_z , which is sometimes called "dipolarizing flux bundle" (DFB) (Liu et al., 2013). These events tend to be associated with fast earthward flow bursts. Their properties have been the subject of many recent studies, both observationally (e.g., Apatenkov et al., 2007; Fu et al., 2011; Li et al., 2011; Runov, Angelopoulos, Sitnov et al., 2011; Runov, Angelopoulos, Zhou et al., 2011; Runov et al., 2009; Runov et al., 2012; Sergeev et al., 2009; Zhou et al., 2009, 2014) and through local (e.g., Birn et al., 2004, 2011) and global magnetohydrodynamic (MHD) simulations (e.g., El-Alaoui et al., 2013, 2016; Ge et al., 2011, 2012; Wiltberger et al., 2015).

The observations have demonstrated a finite cross-tail extent of dipolarization fronts and associated flow bursts, shown also in the 3-D MHD simulations. The MHD simulations have further shown that the DFBs are typically related to local depletions of field line entropy *S*, which may be defined as (e.g., Birn et al., 2009)

$$S = \int P^{1/\gamma} \frac{\mathrm{d}s}{B},\tag{1}$$

where P is the plasma pressure and the integral is taken along closed filed lines. In equilibrium, $S = P^{1/\gamma}V$, where

$$V = \int \frac{\mathrm{ds}}{B} \tag{2}$$

is the differential flux tube volume (e.g., Wolf et al., 2009). The reduction of *S* is thought to be essential in the earthward propagation of the depleted flux tubes, which are also called "bubbles," (e.g., Birn et al., 2004, 2009; Pontius & Wolf, 1990; Wolf et al., 2009), by enabling ballooning/interchange type of modes. In these simulations, the entropy reduction was found to be the consequence of reconnection in the near tail that causes the severance of portions of the closed flux tubes and their tailward ejection. Apart from this generation mechanism, equilibria with local entropy depletions have been shown to be unstable to kinetic ballooning/interchange (hereafter B/I) modes, which also produce earthward flows and dipolarization fronts (Pritchett et al., 2014).

©2018. American Geophysical Union. All Rights Reserved.



In contrast to the potential role of B/I type modes in 3-D configurations, two-dimensional particle-in-cell (PIC) simulations of reconnection in stretched current sheets or magnetotail configurations have demonstrated that sharp DFs can also arise ahead of fast flows ejected from a reconnection site that does not involve localization in the dawn-dusk direction (e.g., Birn & Hesse, 2014; Sitnov et al., 2009).

In these studies the entropy depletion and B_z enhancement arise as a dynamic consequence of magnetic reconnection in the tail or some other mechanism. Recently, however, B_z hump configurations have also gained interest because they can apparently alter the stability properties of the magnetotail, which under average or quiet conditions ought to be stable to ideal MHD (Schindler & Birn, 2004) and collisionless tearing modes (e.g., Lembege & Pellat, 1982; Pellat et al., 1991; Pritchett et al., 1991). Sitnov and Schindler (2010), using a 2-D Vlasov energy principle, showed that the tailward B_z gradient, associated with a hump configuration, could make the tail unstable to collisionless tearing. This was confirmed by PIC simulations, first with open boundary conditions (Bessho & Bhattacharjee, 2014; Sitnov et al., 2013) and later for more stringent closed boundaries (Pritchett, 2015). Merkin et al. (2015) investigated the same kind of configurations with 2-D ideal and resistive MHD simulations and confirmed the PIC results. Their simulations also indicated the possibility of an ideal MHD instability, which might arise prior to the onset of reconnection. The apparently unstable cases, however, did not include strictly closed boundaries as imposed in the ideal MHD energy principle (Bernstein et al., 1958). Finally, Merkin and Sitnov (2016) considered analytical properties of magnetotail configurations with a tailward B_z gradient and the relative importance of the "hump" instability and ballooning/interchange that may be stabilized by finite background pressure.

In this paper we therefore reinvestigate the ideal MHD stability of these hump configurations on the basis of our 2-D tail code (Birn et al., 1996) with strictly closed boundary conditions, paying specific attention to the effect of finite background pressure and density. In section 2 we describe the chosen initial states, which are based on an asymptotic tail equilibrium theory (Birn et al., 1975; Schindler, 1972) and include the configurations investigated by Merkin et al. (2015). Section 3 provides some analytical stability properties, which were used to guide the choice of parameters for the simulation studies. In sections 4 and 5 we describe the evolution of unstable cases. This is followed by a description of properties of the unstable modes in section 6, the investigation of background density and pressure in section 7, and an investigation of the effects of varying the initial hump location in section 8.

2. Initial States and Numerical Approach

In the following we use normalized quantities, based on a characteristic magnetic field strength B_c (typically equal to the lobe field strength), a current sheet half-width L_c , and a density ρ_c , which is taken as the difference between lobe and central plasma sheet density, all taken at the near-Earth boundary. Our pressure unit is defined by $P_c = B_c^2/\mu_0$, the velocity $v_c = B_c/\sqrt{\mu_0\rho_c}$, and the electric field $E_c = v_cB_c$.

The two-dimensional initial states are of the same class investigated previously by Bessho and Bhattacharjee (2014), Merkin et al. (2015), Merkin and Sitnov (2016), Pritchett (2015), and Sitnov and Schindler (2010). They are based on an asymptotic tail equilibrium model, representing a generalization of the well-known Harris equilibrium (Schindler, 1972), defined by a flux function A (y component of the vector potential)

$$A = \ln[\beta(x)\cosh\zeta]$$
 with $\zeta = z/\beta(x)$, (3)

such that

$$B_{x} = -\frac{\partial A}{\partial z} = -\frac{1}{\beta(x)} \tanh \zeta \tag{4}$$

and

$$B_{z} = \frac{\partial A}{\partial x} = \frac{\beta'(x)}{\beta(x)} (1 - \zeta \tanh \zeta) \quad \text{with} \quad \beta'(x) = d\beta(x)/dx.$$
 (5)

We note that we use modified magnetospheric coordinates with x pointing tailward, y dawnward, and z northward. The asymptotic theory assumes that B_z values and variations with x are small, of order ϵ , compared to the main field and the variations with z, neglecting terms of order ϵ^2 compared to unity.

The function $\beta(x)$ describes the current sheet half-width, which, within the validity of the asymptotic theory, is a slowly varying function of x. Our first choice is identical to the one investigated by Merkin et al. (2015)

$$\beta = \exp[\epsilon_1 g(x)],$$
 (Case A) (6)



where

$$g(x) = x + (\alpha/\epsilon_2)(1 + \tanh \xi)$$
 with $\xi = \epsilon_2(x - x_0)$, (7)

such that

$$B_{z0}(x) = B_{z}(x, z = 0) = \beta'(x)/\beta = \epsilon_1(1 + \alpha \cosh^{-2} \xi).$$
 (8)

Here x_0 denotes the location of the B_z hump, α its strength, and $1/\epsilon_2$ its width. The hump is superposed on a background B_z proportional to ϵ_1 , which is constant along the x axis.

Our second choice differs by the background field. It is motivated by earlier investigations (e.g., Birn et al., 1975; Hesse & Schindler, 2001; Liu et al., 2014) and appears, without the hump, more realistic for the typical magnetotail

$$\beta = (1 + \epsilon_0 x)^m \exp[(\epsilon_1 \alpha / \epsilon_2)(1 + \tanh \xi)], \quad \text{(Case B)}$$

with ξ defined as before, such that

$$B_{z0}(x) = \frac{\epsilon_0 m}{1 + \epsilon_0 x} + \frac{\epsilon_1 \alpha}{\cosh^2 \xi}.$$
 (10)

We note that B_{z0} for $\alpha=0$ now is a monotonically decreasing function of x, while the current sheet half-width β monotonically increases. We have kept separate parameters α and ϵ_1 for consistency with model A, although they now appear only as product.

3. Analytical Evaluation of Stability Parameters for Cases A and B Simulations

It is useful to evaluate the formal analytical stability properties of the equilibria considered in Cases A and B. The key parameter for the hump instability (also dubbed Magnetic Flux Release Instability by Merkin & Sitnov, 2016) was introduced by Sitnov and Schindler (2010)

$$C_d(x_f, x) = \frac{2}{\pi} \int_0^{y_f} \frac{B_z(x, z = 0)}{B_z(x'(y), z = 0)} \frac{dy}{y^2 + 1}.$$
 (11)

Here x is the point where the stability parameter is evaluated and x_f is the limit of flux tube integration toward the Earth, represented, for example, by the location of the Earth-side boundary in Cases A and B simulations. The variables x', x, and y are related via

$$y(x',x) = \sqrt{\left[\frac{\beta(x)}{\beta(x')}\right]^2 - 1},\tag{12}$$

 $y_f = y(x_f, x)$, and functions $\beta(x)$ are given by equations (6) and (7) for Case A and equation (9) for Case B. Correspondingly, the function $B_z(x, z = 0)$ under the integral in (11) is given by (8) for Case A and by (10) for Case B.

The parameter C_d governs where the energy integral (e.g., equation (10.72) of Schindler, 2007) might assume negative values, and thus permit unstable solutions, based on a Wentzel-Kramers-Brillouin (WKB) approach. This is possible in the MHD limit if C_d^2 exceeds $\gamma=5/3$ where γ is the polytropic index, (correcting a typo in Merkin & Sitnov, 2016, that stated that $C_d=\gamma$ is the instability threshold). Reversely, $C_d^2<\gamma=5/3$ everywhere implies stability. Although the C_d parameter yields only a necessary instability criterion for modes satisfying the short wavelength WKB limit, it is useful to indicate a potentially unstable regime for our numerical studies.

Figure 1 shows the dependence of the C_d parameter on position x for Case A, based on the parameter set

$$x_0 = 28, \quad \epsilon_1 = 0.03, \quad 1/\epsilon_2 = 7.5, \quad \alpha = 3,$$
 (13)

and integrated to the Earth-side boundary $x_{\min} = -30$ of the simulation. The dashed horizontal line corresponds to $C_d^2 = \gamma$, and marks the necessary condition for instability (Merkin & Sitnov, 2016, with the typo corrected). Note that $C_d^2 < 1$ on the earthward side of the hump, whereas the exact analytical value for the Lembege-Pellat equilibrium is $C_d^2 = 1$ (Hurricane et al., 1996; Sitnov & Schindler, 2010). This is because the integration in (11) was terminated at the Earth-side boundary of the simulation box rather than extended to infinity.

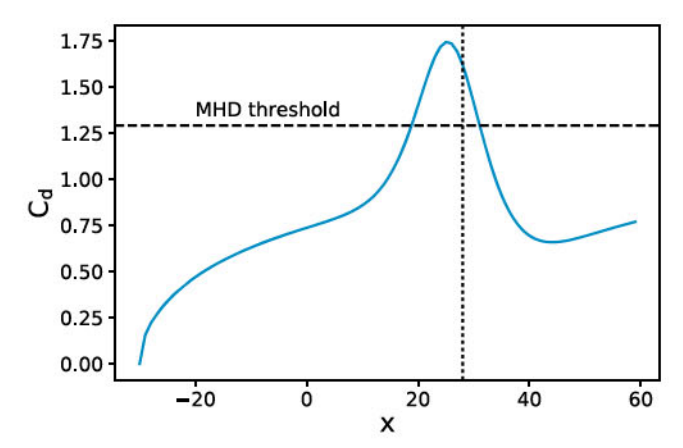


Figure 1. C_d as a function of position x for Case A, assuming integration in (11) is terminated at the Earth-side boundary of the simulation box. The dashed horizontal line marks $C_d^2 = \gamma$, which is the MHD threshold indicating the necessary condition for instability. The dotted vertical line marks $x_0 = 28$, that is, the location of the B_z peak.

Figure 1 indicates that the Case A setup may be unstable, as C_d exceeds the instability threshold in a region around the B_7 peak.

Note that the instability criterion $C_d^2 > \gamma$ neglects the contribution of the background pressure. Further analysis of the energy principle reveals that including a background plasma population yields an updated instability criterion $C_d^2 > \gamma \left(1 + p_b/p_{cs}\right)$, where p_b is the background pressure, while p_{cs} is the pressure in the center of the current sheet that is in equilibrium with the lobe magnetic field. This expression makes it clear that the background should play a stabilizing role, as confirmed by the simulations presented below.

Figure 2 (heavy black line) shows the same dependence of the C_d parameter for Case B, choosing the parameter set

$$\epsilon_0 = 0.05, \quad \epsilon_1 = 0.03, \quad 1/\epsilon_2 = 7.5, \quad \alpha = 3,
x_{\min} = 0, \quad x_0 = 136, \quad m = 0.6.$$
(14)

Additionally, the lighter black lines in Figure 2 also show the variations of C_d for other choices of x_0 , indicated by vertical dashed lines, with the blue dashed line indicating the variation of the maximum values of C_d as function of hump location. (Note that the maximum values are not attained at the hump location itself but slightly to the left.) The dashed orange trace indicates the analytical value of C_d for the Case B equilibrium

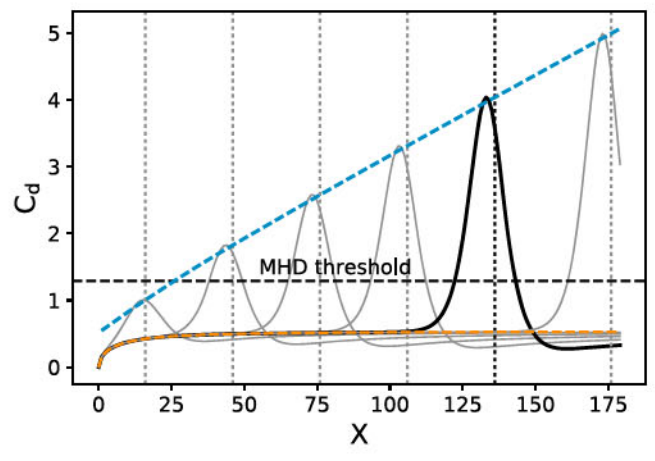


Figure 2. Same as Figure 1 but for Case B with various choices of x_0 , indicated by the dashed vertical lines. The initial choice $x_0 = 136$ is shown by heavy line. The blue line indicates the maximum values of C_d as function of hump location. The dashed orange trace shows the analytical solution for Case B equilibrium without a hump ($\alpha = 0$ in equation (9). The dashed horizontal line shows the MHD stability threshold.



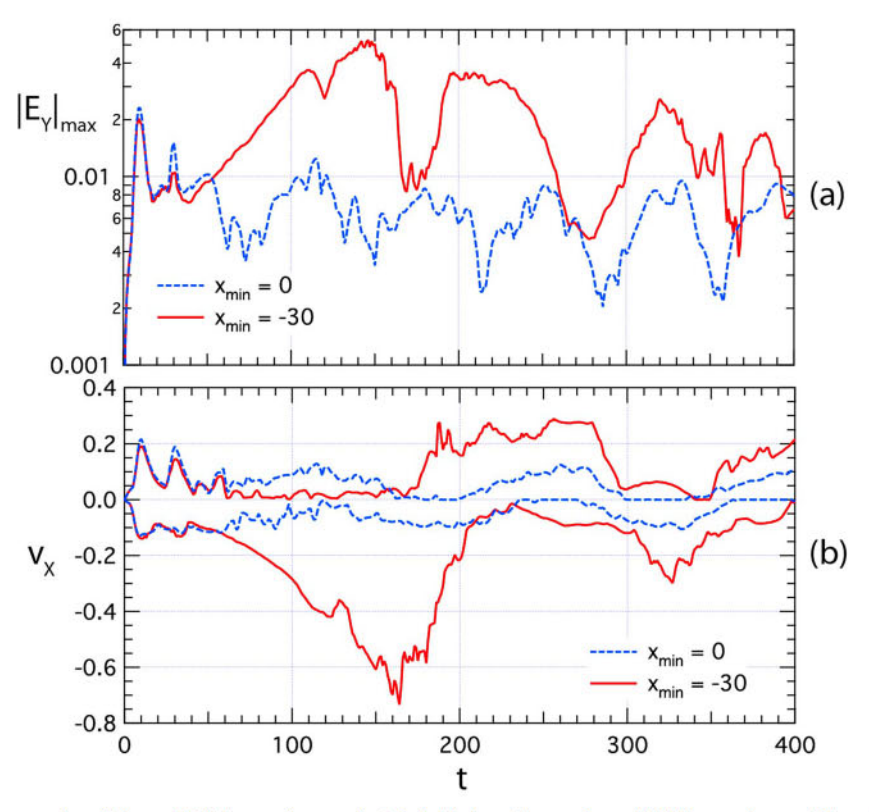


Figure 3. Temporal variations of (a) the maximum electric field along the *x* axis and (b) the maximum tailward and earthward velocities, for Case A with two different locations of the left (earthward) boundary.

without a hump ($\alpha = 0$). In this case, the integral in (11) can be evaluated exactly, and assuming integration to $x_f = 0$ yields

$$C_d(0,x) = \frac{2}{\pi} y(x) {}_2F_1\left(\frac{1}{2}, 1 + \frac{1}{2m}; \frac{3}{2}; -y(x)^2\right),$$
 (15)

where

$$y(x) = \sqrt{(1 + \varepsilon_0 x)^{2m} - 1},\tag{16}$$

and ${}_2F_1$ is the hypergeometric function. The orange trace in Figure 2 corresponds to the right-hand side in (15) and independently verifies the values obtained by numerical integration. As shown in Figure 2, the maximum C_d values remain above the critical threshold for a wide range of hump locations x_0 , indicating a potentially wide range of instability. Initially, we choose a hump location in the more distant tail. However, we will investigate other choices as well in section 8.

4. Evolution of Case A

As a first case we chose parameters consistent with the choices of Merkin et al. (2015) and Merkin and Sitnov (2016), given by (13), with a box slightly extended tailward and outward

$$x_{\text{max}} = 60, \quad z_{\text{max}} = 10$$
 (17)

choosing an inner boundary at $x_{\min}=0$ and a background density $\rho_b=0.2$ (with $p_b=0.1$). This case turned out to be stable. We then extended the left boundary to $x_{\min}=-30$ but kept the normalization to the values at x=0. Since this case was still stable, we lowered the background density and pressure to $\rho_b=0.05$ and $p_b=0.025$, which now yielded instability. This is demonstrated in Figure 3, which shows the temporal variations of the maximum electric field and the maximum tailward and earthward speeds along the x axis as function of time for the two cases with background density $\rho_b=0.05$ but different x_{\min} .

The initial variations of the maximum electric field and the maximum velocities for approximately t < 40 are caused by the deviation from exact equilibrium. The presence of the B_7 hump causes small magnetic pressure

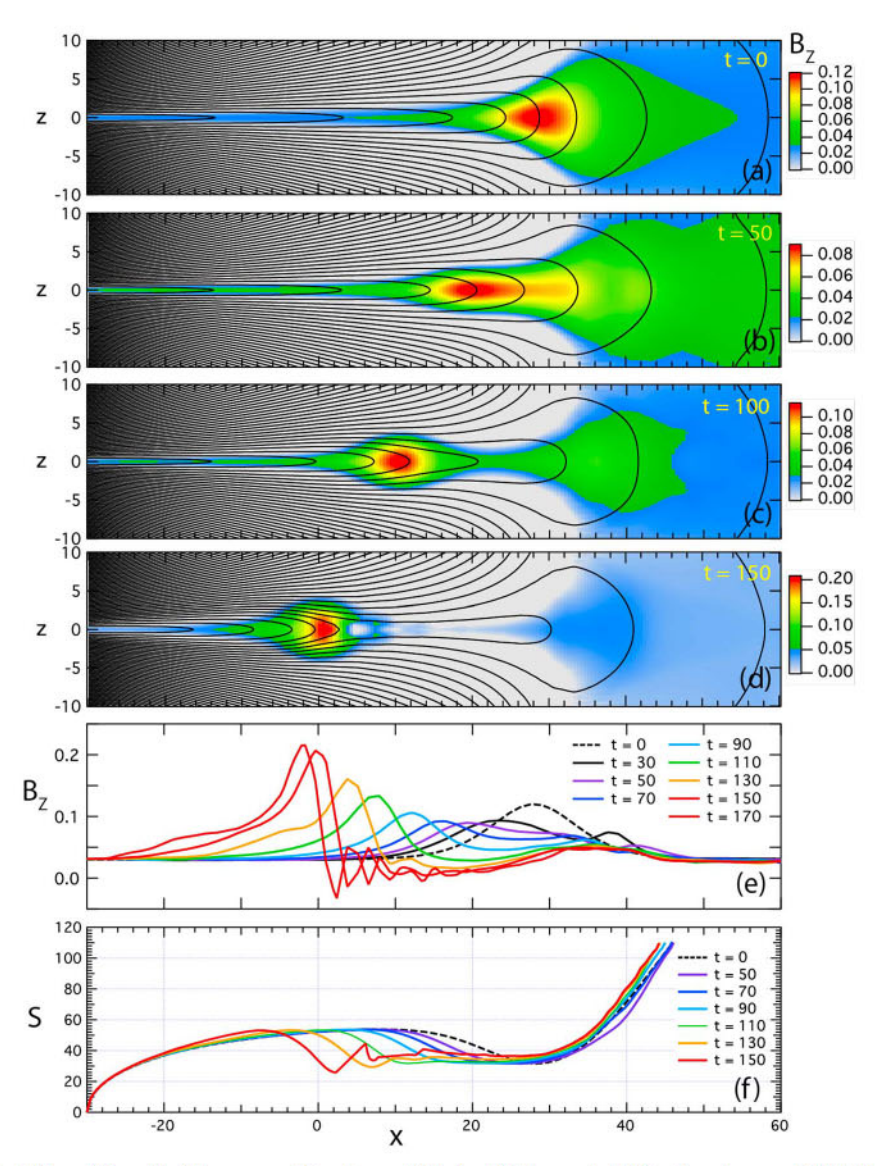


Figure 4. Evolution of Case A with $x_{min} = -30$ and $\rho_b = 0.05$. (a-d) Color-coded $B_z(x, z)$ and magnetic field lines at different times, (e) profile of $B_z(x)$ at z = 0, and (f) the profile of the entropy function S(x), defined by (1), for various times.

forces $\partial B_z^2/\partial x$ of the order of e^3 , which are neglected in the asymptotic equilibrium theory. The fact that the oscillations caused by this initial nonequilibrium are similar for both cases, while only one of them developed instability, is an indication that the later evolution is not related to this initial nonequilibrium. The maximum electric field in the case with $x_{\min} = -30$ (solid red curves) shows a clear, albeit slow compared to a typical Alfvén wave period, exponential growth between about t=50 and t=100, which continues somewhat reduced until $t\approx 150$. This is also shown by the increase in earthward flow speed (negative v_x). This appears to be an indication of linear instability that grows out of an initial perturbation.

This result is a numerical confirmation of the analytical expectation of instability demonstrated in Figure 1, which was obtained without accounting for the background pressure but including the earthward boundary at x = -30. The transition to instability is apparently caused both by the earthward extension of the simulation box and by the reduction of the background pressure or density (section 7). It is worth noting that the background density used by Merkin et al. (2015) in their runs was 0.3 in the units used here for the Case A simulations, while, as Figure 8 indicates, instability requires at least $\rho_b = 0.1$. Thus, the magnetotail configurations presented here are significantly more unstable than those performed by Merkin et al. (2015), and the difference is likely due to the newly revealed effect of the background pressure and/or density.

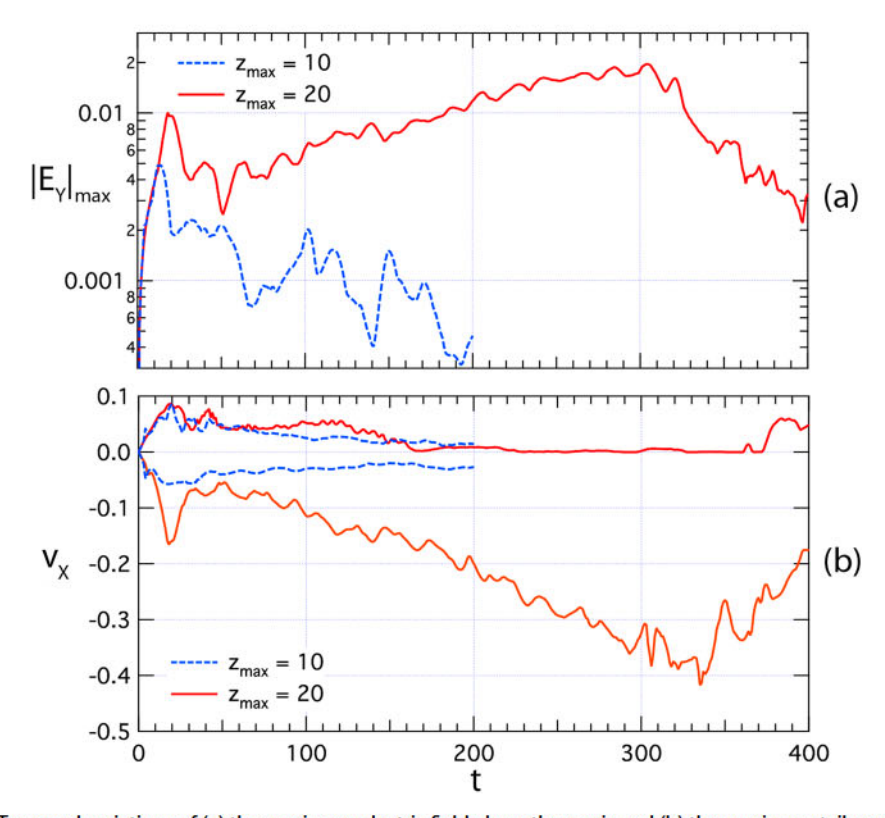


Figure 5. Temporal variations of (a) the maximum electric field along the x axis and (b) the maximum tailward and earthward velocities, for Case B with parameter set (14) and $\rho_b = 0.05$ for two different locations of the outer (z) boundary.

The evolution of the unstable case is further demonstrated in Figure 4, showing (a-d) the color-coded magnitude of B_z in the x, z plane for various times, and (e) $B_z(x)$ at z=0 and (f) the entropy function S(x), defined by (1), at different times. Figure 4 shows the earthward propagation of the B_z hump, documented also in earlier simulations (e.g., Merkin et al., 2015). Figure 4f also shows that the B_z hump is associated with a local reduction of the field line entropy S. It is noteworthy that, except for the initial state, the maximum of B_z does not exactly correspond to the minimum of S but appears to be closer to the steepest earthward gradient. After an initial reduction, the peak in B_z increases as the hump moves earthward. This is obviously an effect of compression, which is absent when the Earth-side boundary is open (Merkin et al., 2015).

5. Evolution of Case B

The background field in Case A already exhibits, for low enough background pressure and sufficiently long tail, a negative gradient of S, which would make it suitable for ballooning instability (Schindler & Birn, 2004). To avoid that we chose the field of Case B, given by (9). Figures 5 and 6 show the evolution for the parameter set (14) with $x_{\text{max}} = 180$ and two locations of the outer boundaries $z = \pm z_{\text{max}}$. Figure 5 shows that not only the earthward boundary but also the outer boundary in z can play a stabilizing role. If this boundary is too close the system remains stable. When it is far enough out, the evolution of the maximum electric field along x again shows, after some initial oscillations, a period of approximately exponential growth.

Figure 6 shows the corresponding evolution of the B_z hump and the related entropy function S for the unstable case. It is similar to that of Case A. We note that at later times the field behind the hump becomes very small, as discussed earlier (Merkin et al., 2015). Due to numerical oscillations B_z may become negative in that region, corresponding to small-scale magnetic islands, which do not permit the evaluation of the entropy integral (1). However, no significant numerical reconnection ensues.



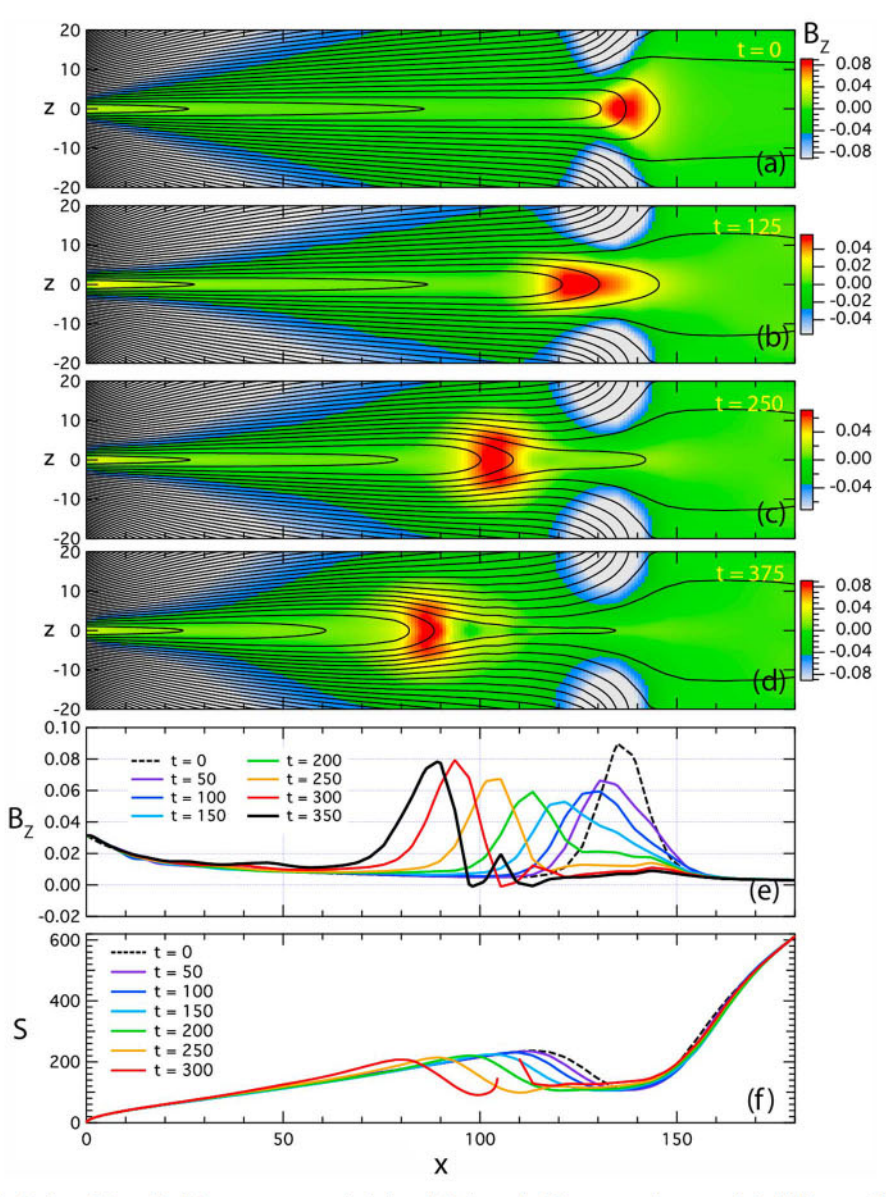


Figure 6. Evolution of Case B with parameter set (14). (a–d) Color-coded $B_z(x, z)$ and magnetic field lines at different times, (e) profile of $B_z(x)$ at z = 0, and (f) the profile of the entropy function S(x), defined by (1), for various times.

6. Mode Characteristics

Figure 7 illustrates, for Case A with a background density $\rho_b = 0.02$ ($p_b = 0.01$), characteristic properties of the fields during the unstable evolution, showing (a) the color-coded magnetic field component B_z ; (b) the flow speed v_x ; (c) the electric field E_y ; and (d) the forces ($\mathbf{J} \times \mathbf{B}$)_x (blue line), $\partial p/\partial x$ (green line), and the net force $F_x = (\mathbf{J} \times \mathbf{B})_x - \partial p/\partial x$, enlarged by a factor of 10 (red dashed line), along the x axis. The time t = 75 was chosen to be late during the exponential growth, so that the mode can be considered to be close to the fastest growing unstable mode. The electric field E_y in Figure 7c then is proportional to the perturbation A_1 of the vector potential, illustrating the solitary character, which has a spatial scale comparable to the B_z hump. The velocity v_x in Figure 7b illustrates the significant earthward extension of the parallel flow speed. Figure 7d demonstrates that the mode is characterized by instantaneous near equilibrium with a net force, which is needed to drive the hump earthward, of the order of e^3 . (Note that F_x in Figure 7d is enlarged by a factor of 10.) This earthward force affects not only the hump but also the region earthward of it, which must collapse as the hump moves earthward.

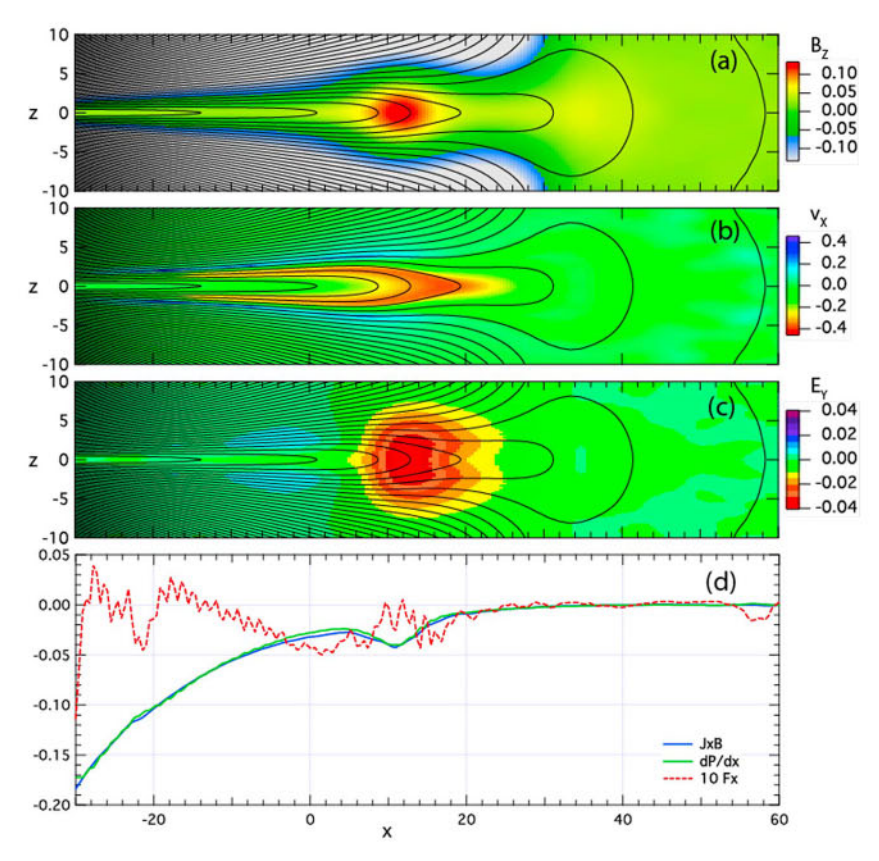


Figure 7. Characteristics of an unstable hump mode for model A with $\rho_b = 0.02$: (a) B_z , (b) v_x , and (c) E_y in the x, z plane, (d) forces along the x axis; the dashed red line shows the net force enlarged by a factor of 10.

7. Influence of Background Density and Pressure

Figure 8 shows the evolution of the location of the B_z hump along the x axis for Cases A and B with various background densities, with the background pressure given as $p_b = \rho_b/2$. The top (black) curve in Figure 8a demonstrates that the case $\rho_b = 0.2$ is stable, as mentioned earlier. In general, the evolution for the unstable Cases A and B shows that it is faster and the penetration of the hump is closer toward Earth, when the background density or pressure is lower. We note that this also corresponds to a lower entropy minimum. This finding is similar to that documented for localized entropy-depleted flux tubes (Birn et al., 2009). However, in the present case this result cannot be attributed to a ballooning or interchange mode, which are excluded by the 2-D assumption.

So far, we have changed the background density and pressure together, so it is not clear which plays the more important role in governing the evolution and penetration of the hump. To discern this we have now changed the background parameters separately. Figure 9 shows the evolution of characteristic quantities as function of time for model A with different background densities and pressures. The red solid curves correspond to the case shown in Figures 3 and 4, and the blue solid curve corresponds to a case for which the background density was enhanced by a factor of 4. The dashed red and blue curves correspond to cases with enhanced background pressure, $p_b = 0.1$. It is obvious that both cases with enhanced pressure (dashed curves) are stable, whereas the lower pressure cases (solid curves) show unstable evolution in a similar way. The density difference affects the speed of the evolution but neither stability nor the depth of penetration of the hump. The difference in the depth of penetration shown in Figures 8a and 8b thus can be attributed to the difference in background pressure rather than density.

The two cases with the same background pressure have the same initial entropy function, whereas the entropy minimum is higher for the case with higher background pressure. Thus, as demonstrated by Figure 10, the depth of penetration may also be considered as governed by the minimum of the entropy function. The

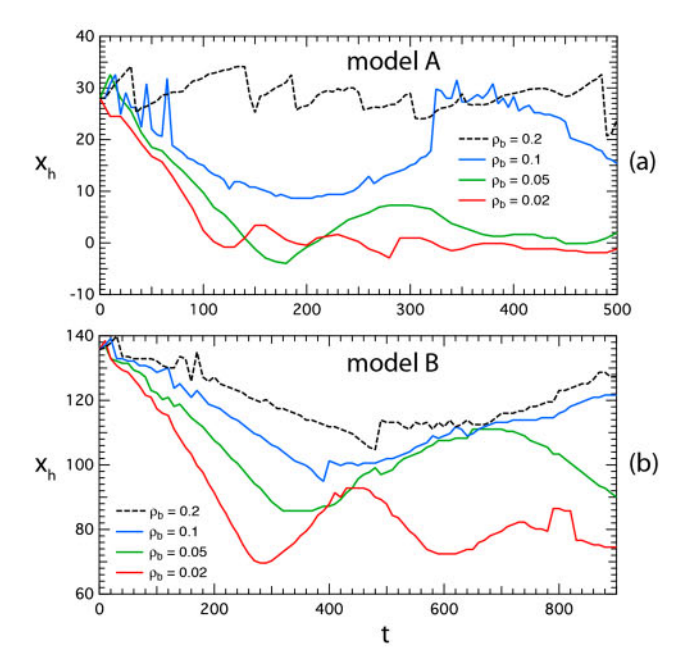


Figure 8. Evolution of the location of the B_Z peak along the x axis for Cases A and B with various background densities (and corresponding background pressures).

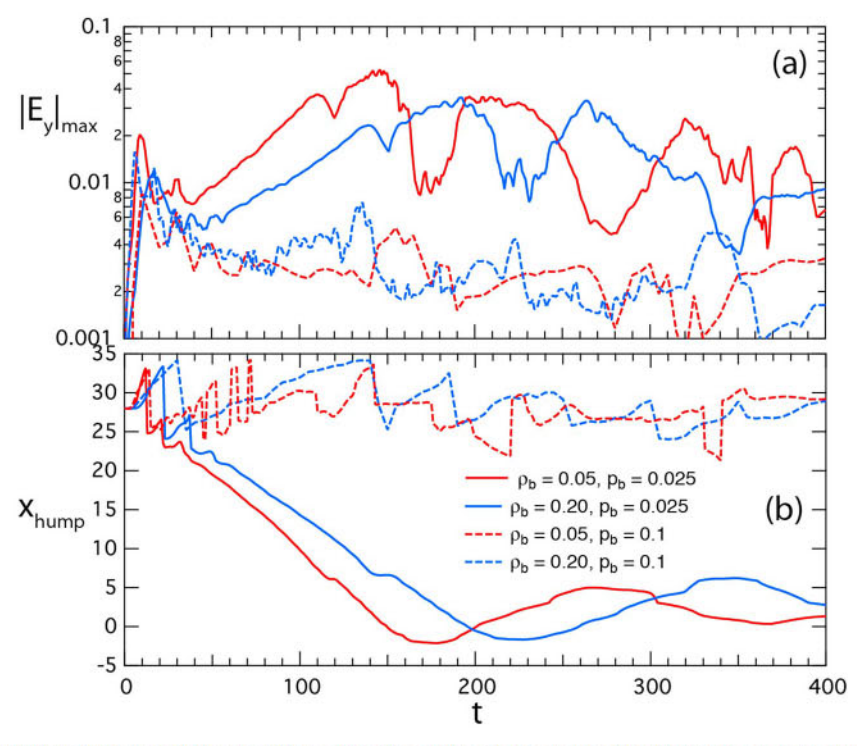


Figure 9. Evolution of characteristic quantities as function of time for model A with different background densities and pressures, (a) the maximum electric field and (b) the location of the B_z peak along the x axis.

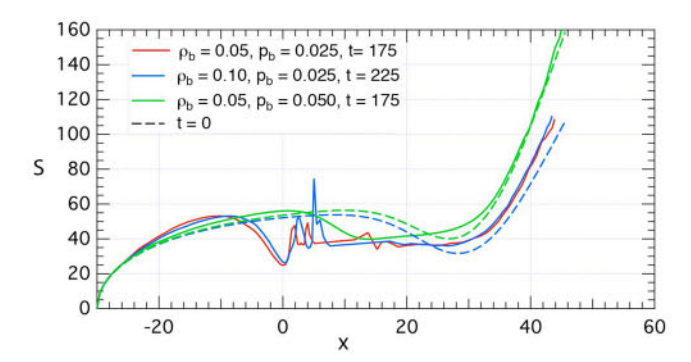


Figure 10. Evolution of the entropy function S(x), as defined by (1), for model A with different background densities and background pressures, shown close to the times of deepest penetration. The dashed lines show the initial distributions.

entropy functions for the two cases with $p_b = 0.025$ at the times of deepest penetration are almost identical. (The local peaks of S just tailward of the minimum are artificial, due to the fact that B_z becomes very small in this region and shows numerical oscillations.)

8. Influence of the Initial Hump Location

The initial locations of the B_z hump were chosen based on the evaluation of the C_d parameter (section 3) and earlier findings (Merkin & Sitnov, 2016) that distant locations should be more likely to become unstable. However, as Figure 2 has indicated for Case B, the maximum value of C_d exceeds the critical threshold for a

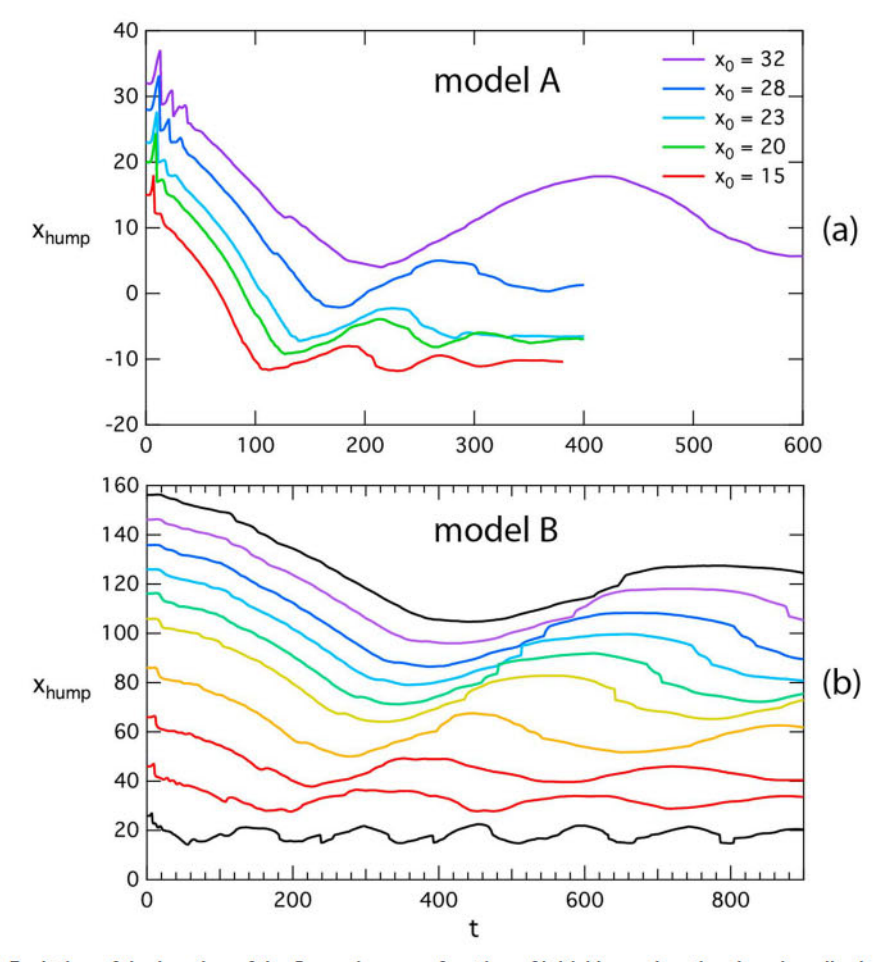


Figure 11. Evolution of the location of the B_Z maximum as function of initial hump location, keeping all other parameters the same, (a) for Case A and (b) for Case B.

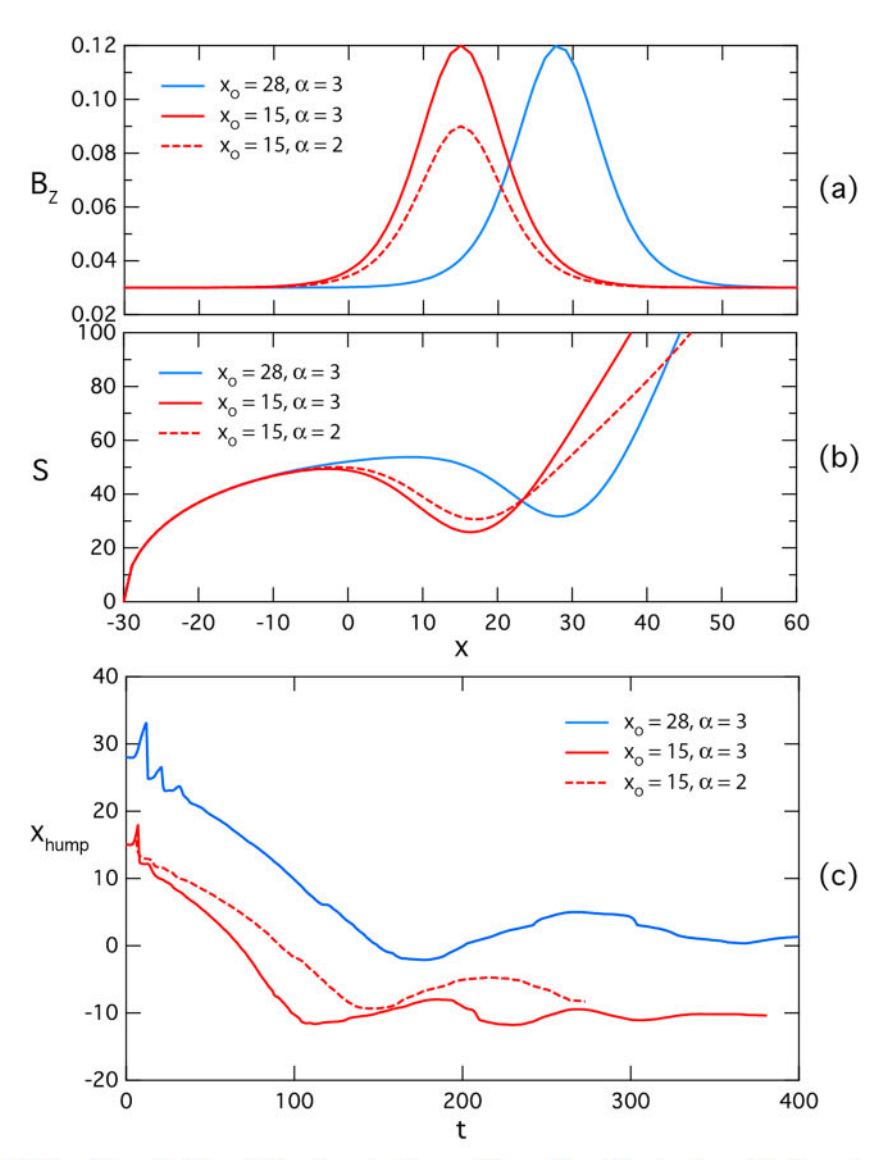


Figure 12. Initial variation of (a) B_z and (b) entropy S with x and (c) evolution of the location of the B_z maximum as function of time for three cases of model A.

wide range of hump locations. We have therefore done a number of runs varying the initial hump location x_0 but keeping all other parameters fixed, as given by (13) and (17) for model A and (14) for model B, choosing $\rho_b = 0.05$ and $\rho_b = 0.025$.

Figure 11 shows the evolution of the hump location for models A and B, demonstrating a wide range of unstable cases. The innermost location, $x_0 = 26$, in Case B shows an apparently stable evolution of oscillation. This is consistent with the conclusion from the C_d parameter in Figure 2.

Figure 11 further indicates that the earthward penetration of the B_z hump (or the entropy minimum) depends on the initial location (although the displacement decreases with decreasing initial distance). This could be due to the fact that the entropy minimum becomes lower for initial humps closer to Earth despite the same B_z hump shape. We have therefore reduced the height of the B_z hump in Case A for the initial location $x_0 = 15$ to obtain the same minimum value of S as for $S_z = 15$ and $S_z = 15$ and $S_z = 15$ shown in Figure 12. Figures 12a and 12b show the initial variation of $S_z = 15$ and $S_z = 15$ and $S_z = 15$ with reduced $S_z = 15$ (red dashed line) still propagates closer to Earth than the hump for $S_z = 15$ (loue line), although not quite as close as for $S_z = 15$ with $S_z = 15$ with



2-D case, is not simply determined by a single parameter, such as the field line entropy S. The hump location, or the shape of the B_2 or S profiles on the earthward side, apparently plays a role as well.

9. Summary and Discussion

Using two-dimensional ideal MHD simulations, we have demonstrated that magnetotail configurations with a local enhancement of B_z , which for small enough background pressure is accompanied by a reduction in field line entropy, can become unstable within the constraints of ideal MHD, even when strict boundary conditions $\mathbf{v}=0$ are imposed at all boundaries, consistent with the constraints of the ideal MHD energy principle (Bernstein et al., 1958). Necessary conditions for instability include the following: (1) The boundary on the earthward side has to be far enough away and the B_z enhancement has to be sufficiently strong. This result has been derived by Merkin and Sitnov (2016) and confirmed here. (2) The high-latitude boundaries also have to be sufficiently far away, while (3) the background pressure, equivalent to the lobe pressure, has to be small enough. The effect of the background pressure is particularly interesting as it additionally controls the strength of the entropy reduction in the B_z enhancement region and thus the relationship of the hump instability with interchange. When the above necessary conditions are met, the unstable evolution then bears strong similarity to the evolution of observed and simulated dipolarized flux bundles and dipolarization fronts, presumed or simulated to be the consequence of reconnection and thus generated in a more dynamic fashion.

We should add here a clarifying remark on the role of background pressure. First of all, when mentioning "background" pressure or density we mean a uniform value added everywhere. This is most noticeable in the open field regions or lobes of the magnetotail. However, the stabilizing or destabilizing effect of background pressure stems particularly from the closed field line region, where a pressure change alters compressibility and thereby possibly stability (e.g., Merkin et al., 2015; Schindler & Birn, 2004). This stabilizing effect was not included in our original evaluation of the C_d parameter in section 3. Preliminary results suggest that a refined stability theory indeed indicates a stabilizing influence of increased pressure.

In order to separate the roles of background pressure p_b and density ρ_b , we have compared cases with identical initial B_z humps but different values of p_b and ρ_b . We found that the stability appeared to be controlled by the pressure alone, similar to B/I modes. Also, lower p_b , equivalent to a lower minimum of S, enables closer penetration to Earth, similar to the case of 3-D localized entropy-depleted flux tubes (Birn et al., 2009). In contrast, the background density had an effect primarily on the speed of the evolution, which is plausible, as it affects the inertia of the plasma to be moved.

Instability was found over a wide range of initial hump locations in x. The B_z hump or entropy-depleted flux bundle was also found to penetrate closer to Earth when the initial location was closer, even when the minimum of the field line entropy S was the same. This shows that, at least in the present 2-D case, the value of the entropy minimum is not the only parameter that determines the hump penetration. The hump location or the shape of the B_z or S profiles on the earthward side apparently plays a role as well.

The simulations start from a configuration that is not in exact equilibrium. This might suggest the possibility that the subsequent evolution is caused by the deviation from equilibrium rather than representing a small-perturbation, linear instability. Two features of the evolution cast doubt on this interpretation. First, a comparison between the stable and unstable cases shows that the early evolution, which is caused by this initial deviation from equilibrium, is very similar, whereas the later evolution becomes different, when apparently an unstable eigenmode grows in the unstable cases. Second, the evolution during the exponential growth can be described as quasi-static, characterized by closeness to instantaneous force balance, such that the net force, which causes an increase in velocities during this phase, is small compared to the ∇P and $\mathbf{J} \times \mathbf{B}$ forces, which approximately balance. If the evolution were caused by the initial force imbalance, one would expect the forces to increase with the deviation from the initial state. However, these arguments are not conclusive, and further investigations are needed to clearly identify the nature of the instability.

Although the simulations demonstrate the possibility of ideal MHD instability of particular magnetotail configurations, they should not be seen as a likely model of the initial onset of tail activity in the near tail. As pointed out by Merkin and Sitnov (2016), and confirmed here, the modes become stabilized if the hump is too close to the Earth, such that it might be a more likely candidate for initiating instability in the more distant tail.



An open question is also how a hump configuration can be set up from an initially stable configuration. Quasi-static equilibrium theory indicates that a local B_z minimum, associated with the formation of a thin embedded current sheet, can be generated by magnetic flux addition and adiabatic (i.e, entropy conserving) compression of the magnetotail (Birn & Schindler, 2002), consistent with some observations of changes during the substorm growth phase (e.g., Sergeev et al., 2018). The adiabatic theory assumption, however, also implies that the entropy function S(x) would remain monotonically increasing with distance, if it did so prior to the deformation. For the presently considered class of stretched tail equilibria, this would imply stability to B/I modes and by implication any 2-D MHD modes as well (Schindler, 2007; Schindler & Birn, 2004).

At present, the most likely, and well documented, mechanism of setup of such B_z humps is magnetic reconnection. An evolution that would redistribute the entropy from an initially stable configuration would likely require a violation of entropy conservation and thus most likely also enable reconnection. In fact, the unstable hump configurations are also unstable to collisionless tearing (Sitnov & Schindler, 2010). This was demonstrated also by PIC simulations, first with open boundary conditions (Bessho & Bhattacharjee, 2014; Sitnov et al., 2013) and later with more rigorous closed boundaries (Pritchett, 2015). In this scenario, the generation of a B_z hump is part of a dynamic evolution, rather than an equilibrium state.

Furthermore, the relevance of the 2-D simulations as models of the actually observed dynamic evolution is reduced by the fact that the local entropy reduction makes the initial states also unstable to 3-D ballooning modes (e.g., Schindler & Birn, 2004). Note that 3-D PIC simulations paint here an intriguingly mixed picture. While some of them (e.g., Pritchett, 2013) clearly show signatures of B/I instability, others (Sitnov et al., 2014) show that the hump instability dominates B/I and other dawn-dusk perturbations (flapping motions) for sufficiently thin current sheets. Thus, further studies, including 3-D MHD simulations, are necessary to clarify the role of the hump instability, its similarity, and difference from the B/I.

The relevance of the present investigation is more of a fundamental nature. It shows that the propagation of DFBs is not necessarily tied to an interchange mode, although a good argument can be made that the 3-D ballooning/interchange makes the evolution faster. Also, in the 2-D case one can no longer argue that the final resting place of the entropy-depleted flux bundle is determined by where its entropy equals that of the surrounding flux tubes in the adjacent cross-tail region. Although we found that the penetration of a DFB is influenced by the entropy depletion, the initial location played a role as well. The earthward motion of the DFB is stopped by a buildup of pressure, which must also be true in the 3-D case. Thus, the pressure (or entropy) content in the closed field region earthward of a hump may be a relevant factor in the stopping as well as in the stabilization. The configuration then oscillates around a final stable state that is apparently governed by the predetermined entropy function S(A), analogous to the evolution in the "Newton challenge" simulations (Birn et al., 2005, 2009).

Acknowledgments

The simulation work was performed at Los Alamos under the auspices of the U.S. Department of Energy, supported by NASA grants NNX13AD10G, NNX13AD21G, and NSF grant 1203711. V. G. M. and M. I. S. would like to acknowledge support from NASA grants NNX13AF82G and NNX15AN73G. We are grateful for the hospitality and support by the International Space Science Institute Bern, Switzerland, and acknowledge the fruitful discussions with Karl Schindler, Michael Hesse, and the members of the ISSI working group. Simulation results are available via http://doi.org/10.5281/zenodo.1212623.

References

Apatenkov, S. V., Sergeev, V. A., Kubyshkina, M. V., Nakamura, R., Baumjohann, W., Runov, A., et al. (2007). Multi-spacecraft observation of plasma dipolarization/injection in the inner magnetosphere. *Annales Geophysicae*, 25(3), 801–814. https://doi.org/10.5194/angeo-25-801-2007

Bernstein, I. B., Frieman, E. A., Kruskal, M. D., & Kulsrud, R. M. (1958). An energy principle for hydromagnetic stability problems. In *Proceedings* of the Royal Society of London. Series A (pp. 17–40). https://doi.org/10.1098/rspa.1958.0023

Bessho, N., & Bhattacharjee, A. (2014). Instability of the current sheet in the Earth's magnetotail with normal magnetic field. *Physics of Plasmas*, 21(1), 102905.

Birn, J., Galsgaard, K., Hesse, M., Hoshino, M., Huba, J., Lapenta, G., et al. (2005). Forced magnetic reconnection. *Geophysical Research Letters*, 32.106105. https://doi.org/10.1029/2004GI.022058

Birn, J., & Hesse, M. (2014). Forced reconnection in the near magnetotail: Onset and energy conversion in PIC and MHD simulations. *Journal of Geophysical Research*: Space Physics, 119, 5497–5505. https://doi.org/10.1002/jgra.50521

Birn, J., Hesse, M., Schindler, K., & Zaharia, S. (2009). Role of entropy in magnetotail dynamics. *Journal of Geophysical Research*, 114, A00D03. https://doi.org/10.1029/2008JA014015

Birn, J., linoya, F., Brackbill, J. U., & Hesse, M. (1996). A comparison of MHD simulations of magnetotail dynamics. *Geophysical Research Letters*, 23. 323–326.

Birn, J., Nakamura, R., Panov, E. V., & Hesse, M. (2011). Bursty bulk flows and dipolarization in MHD simulations of magnetotail reconnection. Journal of Geophysical Research, 116, A01210. https://doi.org/10.1029/2010JA016083

Birn, J., & Schindler, K. (2002). Thin current sheets in the magnetotail and the loss of equilibrium. *Journal of Geophysical Research*, 107(A7), 1117. https://doi.org/10.1029/2001JA0291

Birn, J., Sommer, R. R., & Schindler, K. (1975). Open and closed magnetospheric tail configurations and their stability. Astrophysics and Space Science, 35, 389–402.

Birn, J., Raeder, J., Wang, Y., Wolf, R., & Hesse, M. (2004). On the propagation of bubbles in the geomagnetic tail. *Annales Geophysicae*, 22(5), 1773–1786. https://doi.org/10.5194/angeo-22-1773-2004



- El-Alaoui, M., Richard, R. L., Ashour-Abdalla, M., Goldstein, M. L., & Walker, R. J. (2013). Dipolarization and turbulence in the plasma sheet during a substorm: THEMIS observations and global MHD simulations. *Journal of Geophysical Research: Space Physics*, 118, 7752–7761. https://doi.org/10.1002/2013JA019322
- El-Alaoui, M., Richard, R. L., Nishimura, Y., & Walker, R. J. (2016). Forces driving fast flow channels, dipolarizations, and turbulence in the magnetotail. *Journal of Geophysical Research: Space Physics*, 121, 11,063–11,076. https://doi.org/10.1002/2016JA023139
- Fu, H. S., Khotyaintsev, Y. V., André, M., & Vaivads, A. (2011). Fermi and betatron acceleration of suprathermal electrons behind dipolarization fronts. Geophysical Research Letters, 38, L16104. https://doi.org/10.1029/2011GL048528
- Ge, Y. S., Raeder, J., Angelopoulos, V., Gilson, M. L., & Runov, A. (2011). Interaction of dipolarization fronts within multiple bursty bulk flows in global MHD simulations of a substorm on 27 February 2009. *Journal of Geophysical Research*, 116, A00123. https://doi.org/10.1029/2010JA015758
- Ge, Y. S., Zhou, X.-Z., Liang, J., Raeder, J., Gilson, M. L., Donovan, E., et al. (2012). Dipolarization fronts and associated auroral activities: 1. Conjugate observations and perspectives from global MHD simulations. *Journal of Geophysical Research*, 117, A10226. https://doi.org/10.1029/2012JA017676
- Hesse, M., & Schindler, K. (2001). The onset of magnetic reconnection in the magnetotail. Earth, Planets and Space, 53, 645-653.
- Hurricane, O. A., Pellat, R., & Coroniti, F. V. (1996). Instability of the Lembège-Pellat equilibrium under ideal magnetohydrodynamics. *Physics of Plasmas*, 3(6), 2472–2474. https://doi.org/10.1063/1.871710
- Lembege, B., & Pellat, R. (1982). Stability of a thick two-dimensional quasineutral sheet. *Physics of Fluids*, 25, 1995–2004. https://doi.org/10.1063/1.863677
- Li, S.-S., Angelopoulos, V., Runov, A., Zhou, X.-Z., McFadden, J., Larson, D., et al. (2011). On the force balance around dipolarization fronts within bursty bulk flows. *Journal of Geophysical Research*, 116, A00I35. https://doi.org/10.1029/2010JA01588
- Liu, J., Angelopoulos, V., Runov, A., & Zhou, X.-Z. (2013). On the current sheets surrounding dipolarizing flux bundles in the magnetotail: The case for wedgelets. *Journal of Geophysical Research: Space Physics*, 118, 2000–2020. https://doi.org/10.1002/jgra.50092
- Liu, Y.-H., Birn, J., Daughton, W., Hesse, M., & Schindler, K. (2014). Onset of reconnection in the near magnetotail: PIC simulations. Journal of Geophysical Research: Space Physics, 119, 9773 – 9789. https://doi.org/10.1002/2014JA020492
- Merkin, V. G., & Sitnov, M. I. (2016). Stability of magnetotail equilibria with a tailward B_Z gradient. *Journal of Geophysical Research: Space Physics*, 121, 9411–9426. https://doi.org/10.1002/2016JA023005
- Merkin, V. G., Sitnov, M. I., & Lyon, J. G. (2015). Evolution of generalized two-dimensional magnetotail equilibria in ideal and resistive MHD. Journal of Geophysical Research: Space Physics, 120, 1993–2014. https://doi.org/10.1002/2014JA020651
- Nakamura, R., Baumjohann, W., Klecker, B., Bogdanova, Y., Balogh, A., Rème, H., et al. (2002). Motion of the dipolarization front during a flow burst event observed by Cluster. *Geophysical Research Letters*, 29(4), 1942.
- Pellat, R., Coroniti, F. V., & Pritchett, P. L. (1991). Does ion tearing exist? Geophysical Research Letters, 18, 143–146. https://doi.org/10.1029/91GL00123
- Pritchett, P. L. (2013). The onset of magnetic reconnection in three dimensions. Physics of Plasmas, 20(8), 080703. https://doi.org/10.1063/1.4817961
- Pritchett, P. L. (2015). Instability of current sheets with a localized accumulation of magnetic flux. Physics of Plasmas, 22(6), 062102. https://doi.org/10.1063/1.4921666
- Pritchett, P. L., Coroniti, F. V., & Nishimura, Y. (2014). The kinetic ballooning/interchange instability as a source of dipolarization fronts and auroral streamers. *Journal of Geophysical Research: Space Physics*, 119, 4723–4739. https://doi.org/10.1002/2014JA019890
- Pritchett, P. L., Coroniti, F. V., Pellat, R., & Karimabadi, H. (1991). Collisionless reconnection in two-dimensional magnetotail equilibria. *Journal of Geophysical Research*, 96(A7), 11,523 11,538. https://doi.org/10.1029/91JA01094
- Pontius, D. H. J., & Wolf, R. A. (1990). Transient flux tubes in the terrestrial magnetosphere. *Geophysical Research Letters*, 17, 49–52. https://doi.org/10.1029/GL017i001p00049
- Runov, A., Angelopoulos, V., Sitnov, M. I., Sergeev, V. A., Bonnell, J., McFadden, J. P., et al. (2009). THEMIS observations of an earthward-propagating dipolarization front. Geophysical Research Letters, 36, L14106. https://doi.org/10.1029/2009GL038980
- Runov, A., Angelopoulos, V., Sitnov, M., Sergeev, V. A., Nakamura, R., Nishimura, Y., et al. (2011). Dipolarization fronts in the magnetotail plasma sheet. *Planetary and Space Science*, 59, 517–525. https://doi.org/10.1016/j.pss.2010.06.006
- Runov, A., Angelopoulos, V., & Zhou, X.-Z. (2012). Multipoint observations of dipolarization front formation by magnetotail reconnection. Journal of Geophysical Research, 117, A05230. https://doi.org/10.1029/2011JA017361
- Runov, A., Angelopoulos, V., Zhou, X.-Z., Zhang, X.-J., Li, S., & Plaschke, F. (2011). A THEMIS multicase study of dipolarization fronts in the magnetotail plasma sheet. *Journal of Geophysical Research*, 116, A05216. https://doi.org/10.1029/2010JA016316
- Schindler, K. (1972). A selfconsistent theory of the tail of the magnetosphere. In D. Reidel (Ed.), in Earth's magnetospheric processes, B.M. McCormac (pp. 200–209). Dordrecht-Holland: Astrophysics and Space Science Library.
- Schindler, K. (2007). Space plasma activity. Cambridge, England: Cambridge University Press.
- Schindler, K., & Birn, J. (2004). MHD stability of magnetotail equilibria including a background pressure. Journal of Geophysical Research, 109, A10208. https://doi.org/10.1029/2004JA010537
- Sergeev, V. A., Angelopoulos, V., Apatenkov, S., Bonnell, J., Ergun, R., Angelopoulos, V., et al. (2009). Kinetic structure of the sharp injection/dipolarization front in the flow-braking region. Geophysical Research Letters, 36, L21105. https://doi.org/10.1029/2009GL040658
- Sergeev, V. A., Gordeev, E. I., Merkin, V. G., & Sitnov, M. I. (2018). Does a local B-minimum appear in the tail current sheet during substorm growth phase? Geophysical Research Letters, 45, 2566 – 2573. https://doi.org/10.1002/2018GL077183
- Sitnov, M. I., Buzulukova, N., Swisdak, M., Merkin, V. G., & Moore, T. E. (2013). Spontaneous formation of dipolarization fronts and reconnection onset in the magnetotail. Geophysical Research Letters, 40, 22–27. https://doi.org/10.1029/2012GL054701
- Sitnov, M. I., Merkin, V. G., Swisdak, M., Motoba, T., Buzulukova, N., Moore, T. E., et al. (2014). Magnetic reconnection, buoyancy and flapping motions in magnetotail explosions. *Journal of Geophysical Research: Space Physics*, 119, 7151–7168. https://doi.org/10.1002/2014JA020205
- Sitnov, M. I., & Schindler, K. (2010). Tearing stability of a multiscale magnetotail current sheet. *Geophysical Research Letters*, 37, L08102. https://doi.org/10.1029/2010GL042961
- Sitnov, M. I., Swisdak, M., & Divin, A. V. (2009). Dipolarization fronts as a signature of transient reconnection in the magnetotail. *Journal of Geophysical Research*. 114. A04202. https://doi.org/10.1029/2008JA013980
- Wiltberger, M., Merkin, V., Lyon, J. G., & Ohtani, S. (2015). High-resolution global magnetohydrodynamic simulation of bursty bulk flows. Journal of Geophysical Research: Space Physics, 120, 4555–4566. https://doi.org/10.1002/2015JA021080
- Wolf, R. A., Wan, Y., Xing, X., Zhang, J.-C., & Sazykin, S. (2009). High-resolution global magnetohydrodynamic simulation of bursty bulk flows. Entropy and Plasma Sheet Transport, 114, A00D05. https://doi.org/10.1029/2009JA014044



Zhou, M., Ashour-Abdalla, M., Deng, X., Schriver, D., El-Alaoui, M., & Pang, Y. (2009). THEMIS observation of multiple dipolarization fronts and associated wave characteristics in the near-Earth magnetotail. *Geophysical Research Letters*, 36, L20107. https://doi.org/10.1029/2009GL040663

Zhou, X.-Z., Angelopoulos, V., Liu, J., Runov, A., & Li, S. S. (2014). On the origin of pressure and magnetic perturbations ahead of dipolarization fronts. *Journal of Geophysical Research: Space Physics*, 119, 211–220. https://doi.org/10.1029/2013JA019394

Erratum

In the originally published version of this article, Figure 8 was mistakenly replaced by a copy of Figure 9. The correct Figure 8 has since been substituted, and the present version may be considered the authoritative version of record.